Optics Letters

Integrated optical phased arrays for quasi-Bessel-beam generation

Jelena Notaros,* Christopher V. Poulton, Matthew J. Byrd, Manan Raval, and Michael R. Watts

Research Laboratory of Electronics, Massachusetts Institute of Technology, Cambridge, Massachusetts 02139, USA
**Corresponding author: notaros@mit.edu*

Received 3 July 2017; accepted 3 August 2017; posted 14 August 2017 (Doc. ID 301396); published 1 September 2017

Integrated optical phased arrays for generating quasi-Bessel beams are proposed and experimentally demonstrated in a CMOS-compatible platform. Owing to their elongated central beams, Bessel beams have applications in a range of fields, including multiparticle trapping and laser lithography. In this Letter, continuous Bessel theory is manipulated to formulate the phase and amplitude conditions necessary for generating free-space-propagating Bessel–Gauss beams using on-chip optical phased arrays. Discussion of the effects of select phased array parameters on the generated beam's figures of merit is included. A one-dimensional splitter-tree-based phased array architecture is modified to enable arbitrary passive control of the array's element phase and amplitude distributions. This architecture is used to experimentally demonstrate on-chip quasi-Bessel-beam generation with a ∼14 mm Bessel length and ∼30 μm power full width at half maximum.

OCIS codes: (130.6750) Systems; (130.3120) Integrated optics devices; (140.3300) Laser beam shaping; (350.4855) Optical tweezers or optical manipulation.

https://doi.org/10.1364/OL.42.003510

Bessel beams exhibit many interesting and useful properties [1–4], including propagation of a finite-width central beam without diffraction-induced spreading in the infinite aperture limit [1]. Owing to their unique properties, Bessel beams have contributed to a variety of important applications and advances [5]. For example, they have enabled multiplane, multiparticle optical trapping [6], reduction of scattering and increases in depth of field in microscopy [7,8], efficient laser lithography and fabrication [9], promotion of free-electron laser gain [10], improved laser corneal surgery [11], and adaptive free-space optical communications [12].

In practice, Bessel beams are experimentally approximated by introducing a truncated-Gaussian envelope to the Bessel beam to generate a Bessel–Gauss beam with similar central-beam properties within the Bessel length limit [1–3]. Conventionally, Bessel–Gauss beams have been generated using a bulk optics approach wherein an Axicon lens (a conical glass prism) is illuminated with a truncated-Gaussian beam to produce a Bessel–Gauss beam at the output [3]. Moreover, recent work has turned toward generation of Bessel beams in a more compact form factor. For example, Bessel–Gauss beam generation has been demonstrated using spatial light modulators [13], Dammann gratings [14], slit-groove structures [15], and metasurfaces [16,17]. However, these demonstrations do not provide full on-chip integration, and most are fundamentally limited to static beam formation.

Integrated optical phased arrays, which manipulate and dynamically steer light with large aperture sizes [18] and the potential for 200 MHz rates [19], provide one possible approach to generation of quasi-Bessel beams in a fully integrated platform. However, current phased array demonstrations have focused on systems that form and steer beams or project arbitrary radiation patterns in the far field [18–24]. Near-field manipulation has only recently been explored for holography [25] and focusing applications [26].

In this Letter, integrated optical phased arrays are proposed and demonstrated for the first time as a method for generating quasi-Bessel beams in a fully integrated, compact-form-factor system. First, the phase and amplitude distributions necessary for generating phased-array-based Bessel–Gauss beams are developed analogous to bulk-optics Bessel implementations. Discussion and simulations detailing the effect of the array aperture and phase parameters on the full width at half maximum (FWHM) and Bessel length of the generated beam are included. Next, a splitter-tree-based phased array architecture [18] is modified to passively encode arbitrary phase and amplitude feeding of the array—necessary for Bessel–Gauss-beam generation—and experimental device characterization data are presented. Finally, the developed theory and system architecture are utilized to demonstrate a 0.64 mm × 0.65 mm aperture integrated phased array, which generates a quasi-one-dimensional (quasi-1D) Bessel–Gauss beam with a ∼14 mm Bessel length and ∼30 μm power FWHM. By using a CMOS-compatible platform, the system is naturally scalable to an active demonstration [27] for a fully integrated and steerable chip-based Bessel-beam generator.

In general, a phased array is a system comprising an array of antennas that are fed with controlled phases and amplitudes to generate arbitrary radiation patterns. If the antennas are spaced with a uniform pitch, d, and fed with a Gaussian amplitude and a linear phase distribution [as shown in Figs. 1(a) and 1(b)], the array generates a steerable, diffracting Gaussian beam in the far field of the array. This Gaussian element amplitude distribution is given by

$$A_n = \exp\left(\frac{-4\ln(2)(n - N/2 - 1/2)^2}{(NA_0)^2}\right), \quad (1)$$

where A_n is the amplitude applied to the nth antenna, N is the total number of antennas in the array, and A_0 is the variable amplitude parameter such that the FWHM of the Gaussian is given by NA_0. The near-field electric-field profile generated by this phased array can be approximated by summing the electric-field components of each element in the array:

$$E(x, y, z) = \sum_{n=1}^{N} E_n(x, y, z) \approx \sum_{n=1}^{N} A_n e^{-i(2\pi r_n/\lambda + \Phi_n)}, \quad (2)$$

where Φ_n is the phase applied to the nth antenna, r_n is the distance from the nth antenna to the point under consideration at coordinate (x, y, z), and λ is the propagation wavelength. Using this method, the intensity profile generated by a Gaussian array with $A_0 = 1/2$, $N = 64$, and $d = 10$ μm is simulated, as shown in Fig. 1(c).

In contrast, if an "Axicon-like" element phase distribution is applied in addition to the Gaussian amplitude, the array will generate a quasi-Bessel beam in the near field of the array. This Axicon phase is given by

$$\Phi_n = \Phi_0 \frac{-|n - N/2 - 1/2| + N/2 - 1/2}{N/2 - 1}, \quad (3)$$

where Φ_n is the phase applied to the nth antenna and Φ_0 is the variable phase parameter. This phase can be encoded modulo 2π, as shown in Fig. 1(b). The simulated intensity profiles generated by three 1D Bessel-beam arrays with varying parameters, Φ_0 and A_0, are shown in Figs. 1(d)–1(f). As shown in Fig. 1(f), if the FWHM of the Gaussian element amplitude distribution is too large compared to the aperture size of the array, the integrity of the Bessel–Gauss beam is compromised—the beam formed in Fig. 1(f) is degraded compared to a similar beam in Fig. 1(e). Additionally, because of discretization of the continuous Bessel theory on an array with $d > \lambda/2$, 12 higher-order grating lobes, which also exhibit Bessel properties, are generated by the array at larger angles (not shown in the simulation window).

For potential applications, two valuable figures of merit of a quasi-Bessel-beam-generating array are the power FWHM of the central radiated beam and the Bessel length. Here, the FWHM is calculated in the plane where the power of the central beam is maximally enhanced, and the Bessel length is defined to the point above the array at which the central beam is overcome by the second-order beams and the Bessel approximation breaks down. Similar to bulk implementations, these variables depend on the aperture size of the array and the maximum variation of the Axicon phase, Φ_0. As shown in Figs. 1(g) and 1(h), as the array aperture size increases, the FWHM increases linearly while the Bessel length exhibits quadratic growth. In contrast, as shown in Figs. 1(i) and 1(j), both the FWHM and the Bessel length are related to the phase parameter, Φ_0, through power-law scalings. As such, when considering the application space of the device, it is important to consider the tradeoffs between a long Bessel length versus a small FWHM. For example, if the device is proposed for simultaneous optical trapping of multiple micron-scale particles at varying heights, both a small FWHM and a long Bessel length are desired.

As a proof of concept, a passive quasi-1D Bessel–Gauss-beam-generating integrated optical phased array is designed and fabricated, as shown in Fig. 2(a). The array transmits a Bessel–Gauss beam in the array axis and an exponentially decaying beam in the antenna axis (generation of quasi-1D Bessel beams has been explored [15]). The phased array architecture utilized in the demonstration is based on a silicon-nitride splitting tree [18] with additional components added to enable arbitrary passive control of both the feeding phase and amplitude.

The phased array and accompanying device test structures are fabricated in a CMOS-compatible foundry process at CNSE SUNY on a 300 mm silicon wafer with 6 μm buried oxide thickness. A 200-nm-thick silicon-nitride device layer with 1.95 refractive index at 1550 nm wavelength is deposited

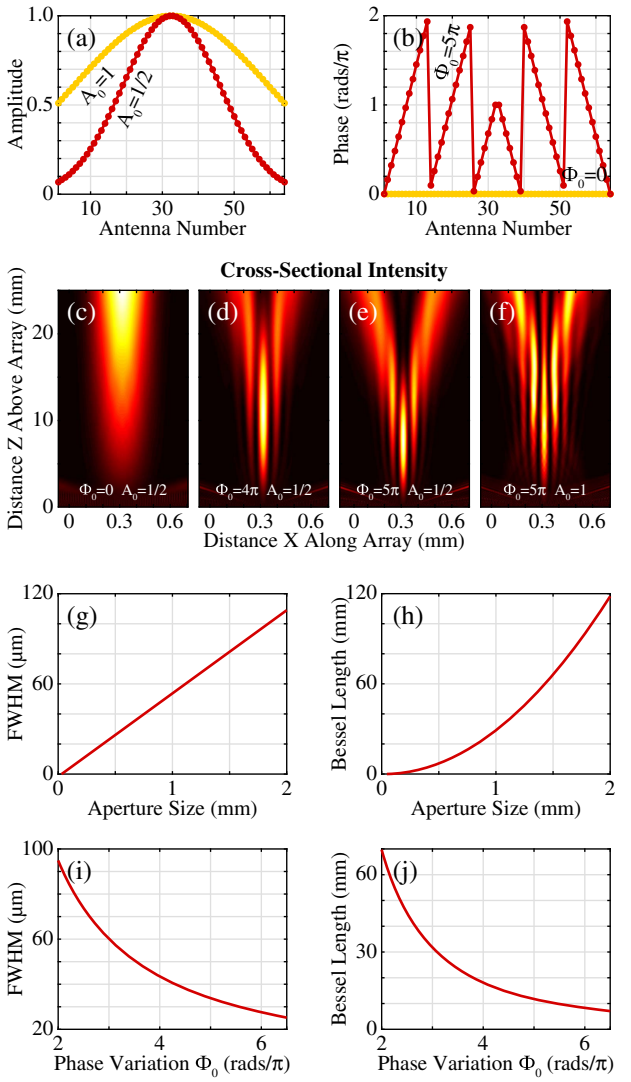

Fig. 1. (a) Element amplitude distribution for a Gaussian-amplitude phased array with $A_0 = 1/2$ (red) and $A_0 = 1$ (yellow). (b) Element phase distribution for a standard (yellow) and Bessel (red) phased array with $\Phi_0 = 0$ and $\Phi_0 = 5\pi$, respectively. Simulated array-factor intensity above the array for a (c) Gaussian array with $\Phi_0 = 0$ and $A_0 = 1/2$, (d) Bessel array with $\Phi_0 = 4\pi$ and $A_0 = 1/2$, (e) Bessel array with $\Phi_0 = 5\pi$ and $A_0 = 1/2$, and (f) distorted Bessel array with $\Phi_0 = 5\pi$ and $A_0 = 1$. (g)–(j) Simulated power FWHM and Bessel length versus array aperture size and maximum element phase variation, Φ_0. Phase profiles and simulated intensities are shown for an array with 64 antennas, 10 μm antenna pitch, and 1550 nm wavelength.

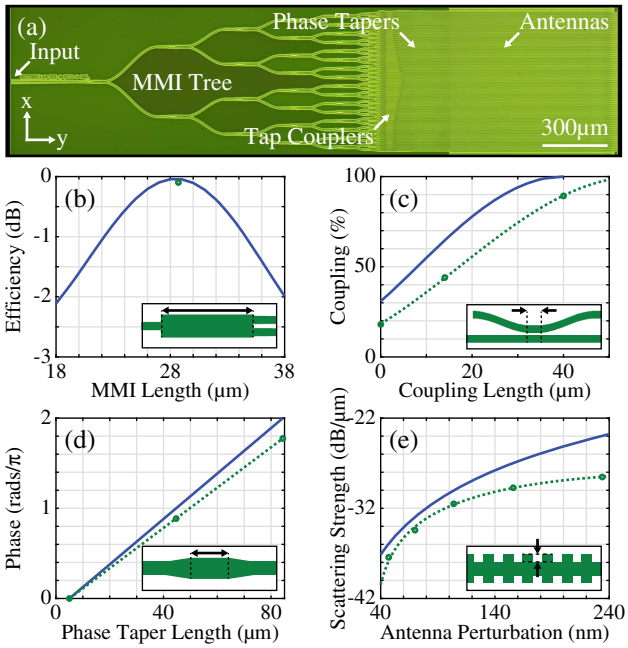

Fig. 2. (a) Micrograph of the fabricated quasi-Bessel-beam-generating phased array. Simulated (blue) and measured (green) (b) efficiency versus MMI device length [18], (c) coupling versus tap coupler length, (d) relative phase versus phase taper length, and (e) scattering strength versus antenna perturbation [18]. Device schematics are included as insets.

using a plasma-enhanced chemical vapor deposition process and patterned using 193 nm immersion lithography.

At the input, an on-chip inverse-taper edge coupler is used to efficiently couple light from a 6.5-μm-mode-field-diameter lensed fiber to a 1.5-μm-wide silicon-nitride waveguide.

Next, a 6-layer multimode-interference (MMI) splitter tree network is used to evenly distribute the input power to 64 waveguide arms with a final pitch of 10 μm. As shown in Fig. 2(b), an MMI is a symmetric 1-to-2-waveguide splitting device based on self-imaging principles [28]. To ensure even splitting with high efficiency, a finite-difference time-domain (FDTD) solver is used to rigorously simulate the device and optimize its geometry for low insertion loss and coupling into the symmetric mode output. As shown in Fig. 2(b), by setting the MMI length to 28.7 μm with a 7 μm MMI width and 2.5-μm-wide input and output waveguides, the simulated and measured insertion losses at the design wavelength are found to be 0.04 dB and less than 0.1 dB, respectively [18].

At the output of the MMI splitter tree, a tap coupler structure [shown in Fig. 2(c)] is placed on each waveguide arm to couple a percentage of the light from each waveguide to a tap port while the remainder of the light in the thru port is routed off the chip (this approach results in inherent power loss, which could be mitigated by using a star-coupler [20] or cascaded [21,22] architecture). As shown in Fig. 2(c), by increasing the length of the coupling region while assuming a 500 nm coupling gap, the input power is sinusoidally coupled from the thru port into the tap port of the device. As such, the length of each tap coupler in the array is chosen to enable a Gaussian feeding amplitude, given by Eq. (1), to the antennas. Although the variation in these coupler lengths induces a nonuniform phase shift on the output ports, the effect on the phase is minimal due to the small waveguide dispersion of the low-index-contrast waveguides and given the noncompounding nature of the splitter-tree-based architecture compared to cascaded implementations [21,22].

On the output tap port of each coupler device, a phase taper structure is placed to impart a static phase delay dependent on the length of the device's wide section. As shown in Fig. 2(d), as the length of the 2.2-μm-wide section of the structure is increased while the 185 μm total length is kept constant, the relative phase induced by the structure increases linearly as predicted by waveguide theory. As such, by choosing the appropriate wide-section lengths for each phase taper, the correct phase profile, given by Eq. (3), is applied. Owing to the modulo 2π phase encoding and the noncompounding architecture, the system is robust to fabrication-induced phase variations.

Finally, after each phase taper, a 650-μm-long grating-based antenna is placed on each arm to create a 0.64 mm × 0.65 mm aperture size. The antennas are designed to radiate perpendicularly out of the plane of the chip and exponentially along the antenna length [18]. By varying the symmetric inward perturbation of the antenna, as shown in Fig. 2(e), the rate of this exponential radiation—i.e., the scattering strength defined as the power radiated by the antenna per unit length—can be controlled. As such, a 200 nm perturbation and 1027 nm period are chosen to reduce the excess power at the end of the 650-μm-long antennas.

To characterize the fabricated array, an optical system is used to simultaneously image the plane of the chip onto a visible camera and an InGaAs IR camera. The height of the optical imaging system is then progressively scanned such that top-down views of the intensity at varying heights above the chip are recorded. These top-down views are then integrated in the antenna axis to visualize the cross-sectional intensity as a function of the distance above the chip.

The resulting cross-sectional intensity as a function of the distance above the chip and three top-down views are shown in Figs. 3(a)–3(d) for the fabricated quasi-Bessel-beam-generating array with $\Phi_0 = 5\pi$ and $A_0 = \sqrt{2}/2$. In the plane of the chip [Fig. 3(d)], the aperture is illuminated by the antennas. As the system scans through the Bessel region of the beam [Fig. 3(c)], a characteristic 1D Bessel–Gauss beam is observed with an elongated yet narrow central beam. In this region, a central-beam FWHM of ~30 μm is measured along the Bessel length, closely matching the simulated value of 30.7 μm. Finally, above the Bessel length [Fig. 3(b)], the central beam is destroyed, the Bessel breaks down, and the light begins diffracting outwards. The measured Bessel length of ~14 mm is slightly longer than the simulated value of 11.4 mm. This deviation can be attributed to the imperfect performance of the tap couplers [as shown in Fig. 2(c)] deforming the feeding amplitude profile of the device.

Next, an 18-μm-diameter gold wire is placed in the path of the central beam along the antenna axis 7.5 mm above the chip. The resulting cross-sectional intensity as a function of the distance above the chip and three top-down views are shown in Figs. 3(e)–3(h). As shown in Fig. 3(h), the wire obstructs the central beam. However, the central beam reforms after a shadow-zone length and continues to propagate with its characteristic elongated profile even after obstruction, as shown in Fig. 3(f).

In summary, this work presents the first proposal and demonstration of integrated optical phased arrays that generate quasi-Bessel beams in the near field of the array. The phases and amplitudes necessary for Bessel–Gauss beam generation, and relevant variables and parameters have been presented

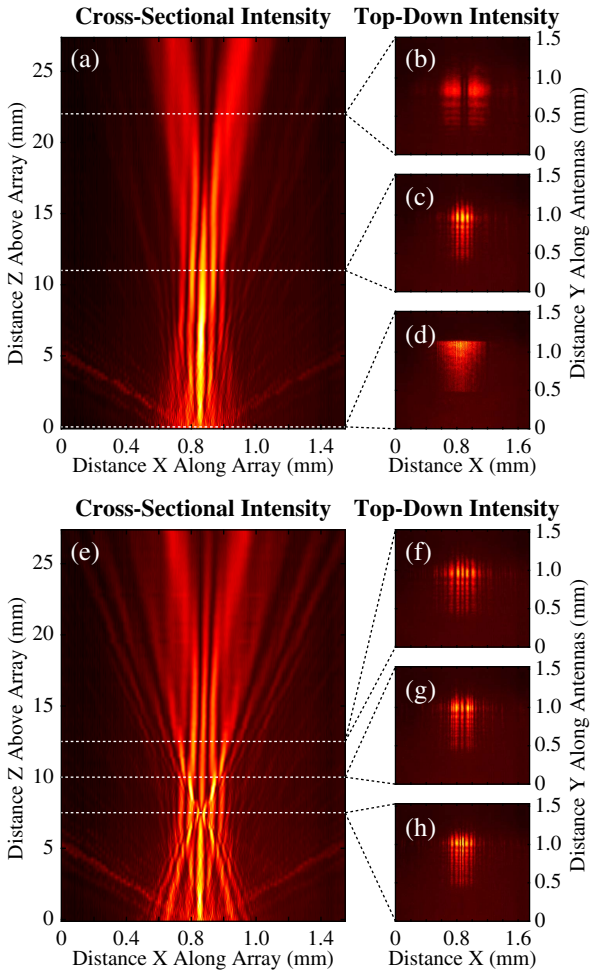

Fig. 3. (a) Measured cross-sectional intensity (in dB) above the chip for a quasi-Bessel-beam-generating phased array with top-down intensity shown (d) in the plane of the chip ($z = 0$ mm), (c) within the Bessel region of the emitted beam ($z = 11$ mm), and (b) after breakdown of the Bessel region ($z = 22$ mm). (e) Measured cross-sectional intensity (in dB) for the generated quasi-Bessel beam when obstructed by a gold wire. Top-down intensities are shown (h) in the plane of the obstacle ($z = 7.5$ mm), (g) within the shadow zone of the obstacle ($z = 10$ mm), and (f) after reformation of the central beam ($z = 12.5$ mm).

and discussed. A new arbitrary phase- and amplitude-controlled splitter-tree-based architecture has been developed and experimental device results have been shown. The array architecture has been used to experimentally demonstrate a quasi-Bessel-beam-generating array closely matching simulation with a ~14 mm Bessel length and ~30 μm power FWHM. Owing to the elongated properties of Bessel–Gauss beams, this on-chip system has important applications ranging from multiparticle optical trapping to scalable laser lithography.

Since the array is fabricated in a CMOS-compatible platform, it is naturally scalable to an active fully integrated system with angular-steering capabilities through interfacing with active silicon-based phase shifters [27]. Additionally, 2D Bessel–Gauss-beam generation can be achieved either by appropriately shaping the phase and amplitude characteristics of the antennas in the splitter-tree-based array (through apodization of the period and perturbation strength along the antenna [29]) or by using a 2D emitter-based architecture [22]. Furthermore, the loss naturally induced by the tap coupler amplitude approach in the array can be eliminated by using either a star coupler, which simultaneously splits the signal and imparts a Gaussian amplitude profile [20], or a cascaded bus architecture with serial taps [21,22]. Finally, the demonstration can be scaled to larger aperture sizes to enable longer Bessel lengths; for example, assuming the 4 mm aperture previously demonstrated in this platform [18], a 0.48 m Bessel length could be demonstrated.

Funding. Defense Advanced Research Projects Agency (DARPA) (HR0011-12-2-0007); National Science Foundation (NSF) (1122374).

Acknowledgment. The authors thank Diedrik Vermeulen for coordinating the top-level mask assembly.

REFERENCES

1. J. Durnin, J. Opt. Soc. Am. A **4**, 651 (1987).
2. F. Gori, G. Guattari, and C. Padovani, Opt. Commun. **64**, 491 (1987).
3. Z. Bouchal, J. Wagner, and M. Chlup, Opt. Commun. **151**, 207 (1998).
4. J. Chen, J. Ng, Z. Lin, and C. Chan, Nat. Photonics **5**, 531 (2011).
5. D. McGloin and K. Dholakia, Contemp. Phys. **46**, 15 (2005).
6. V. Garces-Chavez, D. McGloin, H. Melville, W. Sibbett, and K. Dholakia, Nature **419**, 145 (2002).
7. F. O. Fahrbach, P. Simon, and A. Rohrbach, Nat. Photonics **4**, 780 (2010).
8. P. Dufour, M. Piché, Y. De Koninck, and N. McCarthy, Appl. Opt. **45**, 9246 (2006).
9. L. Yang, S. Ji, K. Xie, W. Du, B. Liu, Y. Hu, J. Li, G. Zhao, D. Wu, W. Huang, S. Liu, H. Jiang, and J. Chu, Opt. Express **25**, 8144 (2017).
10. D. Li, K. Imasaki, S. Miyamoto, S. Amano, and T. Mochizuki, Int. J. Infrared Millim. Waves **27**, 165 (2006).
11. O. Ren and R. Birngruber, IEEE J. Quantum Electron. **26**, 2305 (1990).
12. S. Li and J. Wang, Sci. Rep. **7**, 43233 (2017).
13. N. Chattrapiban, E. A. Rogers, D. Cofield, W. T. Hill III, and R. Roy, Opt. Lett. **28**, 2183 (2003).
14. P. García-Martínez, M. M. Sánchez-López, J. A. Davis, D. M. Cottrell, D. Sand, and I. Moreno, Appl. Opt. **51**, 1375 (2012).
15. S. Kang and K. Oh, Opt. Commun. **284**, 5388 (2011).
16. X. Li, M. Pu, Z. Zhao, X. Ma, J. Jin, Y. Wang, P. Gao, and X. Luo, Sci. Rep. **6**, 20524 (2016).
17. W. T. Chen, M. Khorasaninejad, A. Y. Zhu, J. Oh, R. C. Devlin, A. Zaidi, and F. Capasso, Light Sci. Appl. **6**, e16259 (2017).
18. C. V. Poulton, M. J. Byrd, M. Raval, Z. Su, N. Li, E. Timurdogan, D. Coolbaugh, D. Vermeulen, and M. R. Watts, Opt. Lett. **42**, 21 (2017).
19. F. Aflatouni, B. Abiri, A. Rekhi, and A. Hajimiri, Opt. Express **23**, 21012 (2015).
20. D. N. Hutchison, J. Sun, J. K. Doylend, R. Kumar, J. Heck, W. Kim, C. T. Phare, A. Feshali, and H. Rong, Optica **3**, 887 (2016).
21. A. Yaacobi, J. Sun, M. Moresco, G. Leake, D. Coolbaugh, and M. R. Watts, Opt. Lett. **39**, 4575 (2014).
22. J. Sun, E. Timurdogan, A. Yaacobi, E. S. Hosseini, and M. R. Watts, Nature **493**, 195 (2013).
23. J. Hulme, J. Doylend, M. Heck, J. Peters, M. Davenport, J. Bovington, L. Coldren, and J. Bowers, Opt. Express **23**, 5861 (2015).
24. S. Chung, H. Abediasl, and H. Hashemi, in *IEEE International Solid-State Circuits Conference (ISSCC)* (IEEE, 2017), pp. 262–263.
25. J. Zhou, J. Sun, A. Yaacobi, C. V. Poulton, and M. Watts, *Integrated Photonics Research, Silicon and Nanophotonics* (OSA, 2015), paper IT4A.7.
26. J. Notaros, C. Poulton, M. Raval, M. Byrd, D. Coolbaugh, and M. Watts, in *Conference on Lasers and Electro-optics (CLEO): Science and Innovations* (OSA, 2017), paper STh1M.3.
27. M. R. Watts, J. Sun, C. DeRose, D. C. Trotter, R. W. Young, and G. N. Nielson, Opt. Lett. **38**, 733 (2013).
28. L. B. Soldano and E. C. Pennings, J. Lightwave Technol. **13**, 615 (1995).
29. J. Notaros, F. Pavanello, M. T. Wade, C. Gentry, A. Atabaki, L. Alloatti, R. J. Ram, and M. Popovic, in *Optical Fiber Communication Conference* (OSA, 2016), paper M2I.5.